nature energy

Article

https://doi.org/10.1038/s41560-022-01188-2

Energy- and carbon-efficient CO_2/CO electrolysis to multicarbon products via asymmetric ion migration–adsorption

Received: 1 March 2022

Accepted: 9 December 2022

Adnan Ozden[1,7], **Jun Li**[1,2,3,7] ✉, **Sharath Kandambeth**[4,7], **Xiao-Yan Li**[2,7], **Shijie Liu**[1], **Osama Shekhah**[4], **Pengfei Ou**[2], **Y. Zou Finfrock**[5], **Ya-Kun Wang**[2], **Tartela Alkayyali**[1], **F. Pelayo García de Arquer**[6], **Vinayak S. Kale**[4], **Prashant M. Bhatt**[4], **Alexander H. Ip**[2], **Mohamed Eddaoudi**[4] ✉, **Edward H. Sargent**[2] ✉ & **David Sinton**[1] ✉

Carbon dioxide/monoxide (CO_2/CO) electrolysis provides a means to convert emissions into multicarbon products. However, impractical energy and carbon efficiencies limit current systems. Here we show that these inefficiencies originate from uncontrolled gas/ion distributions in the local reaction environment. Understanding of the flows of cations and anions motivated us to seek a route to block cation migration to the catalyst surface—a strategy we instantiate using a covalent organic framework (COF) in bulk heterojunction with a catalyst. The π-conjugated hydrophobic COFs constrain cation (potassium) diffusion via cation–π interactions, while promoting anion (hydroxide) and gaseous feedstock adsorption on the catalyst surface. As a result, a COF-mediated catalyst enables electrosynthesis of multicarbon products from CO for 200 h at a single-pass carbon efficiency of 95%, an energy efficiency of 40% and a current density of 240 mA cm^{-2}.

The electrochemical reduction of CO_2 and CO (CO_2RR/CORR)—powered by renewable electricity—provides a route to upgrade captured CO_2 into multicarbon (C_{2+}) products[1–5]. Present-day CO_2RR/CORR technology realizes the production of C_{2+} products such as ethylene, ethanol and *n*-propanol at notable rates (>100 mA cm^{-2})[6–8]. The challenge is to achieve these productivities with viable energy efficiency (EE) and carbon efficiency (equivalent to single-pass carbon efficiency (SPCE) in the state-of-the-art, once-through electrolysers)[9–12]. Progress here will require innovative material and system design principles that enable practical EE and SPCE in the electrosynthesis of C_{2+} products[13–16].

Alkaline electrolytes enable absolute potentials (voltage versus standard hydrogen electrode) to be applied under the conditions that minimize the driving force for proton-coupled electron transfer, promoting carbon–carbon (C–C) coupling[17,18]—a rate-limiting step along the pathway to C_{2+} products[3]. With recent advances in catalyst and electrolyser designs, alkaline media CO_2RR achieves an impressive $EE_{C_{2+}}$ of 40% (Fig. 1a), moving EEs towards the realm of industrial viability (>50% $EE_{C_{2+}}$)[17,19]. However, in alkaline electrolytes, CO_2 reacts with hydroxide to form (bi)carbonate, limiting the $SPCE_{C_{2+}}$ to <5%[16].

---

[1] Department of Mechanical and Industrial Engineering, University of Toronto, Toronto, Ontario, Canada. [2] Department of Electrical and Computer Engineering, University of Toronto, Toronto, Ontario, Canada. [3] Frontiers Science Center for Transformative Molecules, Shanghai Jiao Tong University, Shanghai, China. [4] Division of Physical Sciences and Engineering, Advanced Membranes and Porous Materials Center, Functional Materials Design, Discovery and Development Research Group, King Abdullah University of Science and Technology, Thuwal, Kingdom of Saudi Arabia. [5] Structural Biology Center, X-Ray Science Division, Argonne National Laboratory, Lemont, IL, USA. [6] ICFO – Institut de Ciències Fotòniques, The Barcelona Institute of Science and Technology, Barcelona, Spain. [7] These authors contributed equally: Adnan Ozden, Jun Li, Sharath Kandambeth, Xiao-Yan Li. ✉e-mail: lijun001@sjtu.edu.cn; mohamed.eddaoudi@kaust.edu.sa; ted.sargent@utoronto.ca; sinton@mie.utoronto.ca

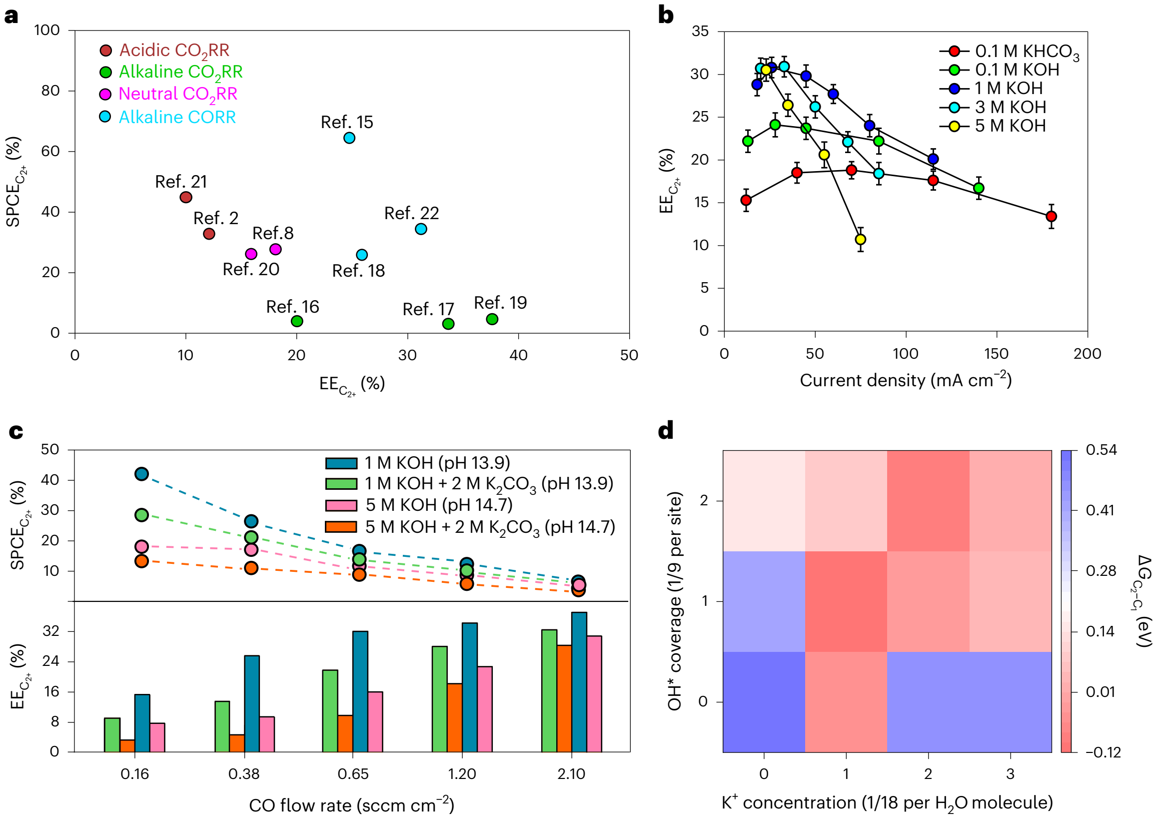

Fig. 1 | Energy and carbon efficiency limitations in CO_2/CO electrolysis. **a**, $EE_{C_{2+}}$ and $SPCE_{C_{2+}}$ performance assessment of literature benchmark CO_2RR/CORR systems. Acidic CO_2RR systems are reported in refs. 2, 21, neutral CO_2RR systems are reported in refs. 8, 20, alkaline CO_2RR systems are reported in refs. 16, 17, 19 and alkaline CORR systems are reported in refs. 15, 18, 22. **b**, $EE_{C_{2+}}$ performances of bare Cu catalyst with anolytes of various pH values in a zero-gap, catholyte-free MEA electrolyser at a constant CO feedstock flow rate of ~1 sccm cm^{-2}. The error bars represent the s.d. of three independent measurements. The data are presented as mean values ± s.d. **c**, Effect of K^+ and OH^- concentration on the $EE_{C_{2+}}$ and $SPCE_{C_{2+}}$ performances of bare Cu catalysts at various CO feedstock flow rates (5 M KOH (pH 14.7), 1 M KOH (pH 13.9), 5 M KOH + 2 M K_2CO_3 (pH 14.7) and 1 M KOH + 2 M K_2CO_3 (pH 13.9)). **d**, A map of free energy differences ($\Delta G_{C_2-C_1} = (\Delta G^{C_2}_{OCCOH^*-(2CO^*+H^++e^-)} - \Delta G^{C_1}_{CHO^*-(CO^*+H^++e^-)})$) for CO reduction to OCCOH* and CHO* at various K^+ concentrations and OH* coverages. In this correlation, $\Delta G^{C_2}_{OCCOH^*-(2CO^*+H^++e^-)}$ is the Gibbs free energy difference of OCCOH* and 2CO* + H^+ + e^- for the C_2 formation pathway and $\Delta G^{C_1}_{CHO^*-(CO^*+H^++e^-)}$ is the Gibbs free energy difference of CHO* and CO* + H^+ + e^- for the C_1 formation pathway. A low $\Delta G_{C_2-C_1}$ value indicates conditions favourable for C_2 production.

The use of neutral electrolytes enables a higher $SPCE_{C_{2+}}$ of ~30%, but this comes at the expense of a lower $EE_{C_{2+}}$ of <20%[20] (Fig. 1a). Acidic electrolytes regenerate CO_2 locally, offering a carbon-efficient platform for CO_2RR. However, promoting CO_2RR in acidic electrolytes is a challenge, with C–C coupling less favoured[2,21]. indeed, the best previous acidic CO_2RR has an $EE_{C_{2+}}$ of ~10% (Fig. 1a)[2]. The present-day trade-off between $EE_{C_{2+}}$ and $SPCE_{C_{2+}}$ highlights the need for strategies that enable high EE and SPCE simultaneously.

Cascade CO_2RR–CO_2 reduction to CO in a carbon-efficient system and CO reduction to C_{2+} in an alkaline system—offers one such avenue: it delivers competitive $EE_{C_{2+}}$ to single-step CO_2RR with the benefit of a higher $SPCE_{C_{2+}}$ (Fig. 1a)[22]. Since present-day CO_2-to-CO conversion systems (such as solid oxide electrolysers) are industrially mature in terms of EE (>85% without heat) and SPCE (45%)[22], it is the CORR to C_{2+} that has the greatest opportunity to improve further[4]. Recent advances in electrolyser configurations[15], electrode–electrolyte interface[18] and catalyst microenvironments[22] have led to encouraging 32% $EE_{C_{2+}}$ combined, simultaneously, with 43% $SPCE_{C_{2+}}$.

Herein, we sought to understand the origins of low $EE_{C_{2+}}$ and $SPCE_{C_{2+}}$ in the best current zero-gap CO_2RR/CORR electrolysers. We found that cations (K^+) cross over from the anode to the cathode, accumulate on the catalyst surface, block the active sites, limit CO adsorption and lead to hydrogen evolution reaction (HER)—the primary cause of low EE and SPCE. An additional cause is OH^- migration from the cathode to the anode, reducing alkalinity on the cathode and thereby diminishing C–C coupling—a key step along the pathway to C_{2+} products. We therefore developed a strategy to break the bidirectional flow of ions (that is, to repel the cations (K^+) while attracting locally generated anions (OH^-)). We implemented this concept with a catalyst/covalent organic framework (COF) bulk heterojunction (CCBH) that provides asymmetric ion migration–adsorption (AIM–A). The π-conjugated hydrophobic COFs constrain cation (K^+) diffusion via cation–π interactions while promoting the adsorption of anion (OH^-) and gas reactant on the catalyst surface. As a result, we achieved electrosynthesis of C_{2+} products with a $SPCE_{C_{2+}}$ of 95% and an $EE_{C_{2+}}$ of 41%, all sustained over 200 h at a constant current density of 240 mA cm^{-2}.

Analysis of energy and carbon efficiency

A recent energy assessment of ethylene electroproduction has pointed to a target energy intensity of 80 GJ per tonne of ethylene[23]. This target intensity is based on ethylene's lower heating value and a minimum total process efficiency of 60%[23]. Accordingly, we sought to investigate the EE and SPCE combinations that could achieve commercial viability. Our analysis considered high-rate and perfectly selective production of ethylene (Supplementary Note 1), which is a signature CORR product and requires gas phase separation[22]. This high-level analysis showed that further advancements in EE and SPCE are critical to achieve practical electrosynthesis of C_{2+} (that is, ethylene) via cascade CO_2RR (Supplementary Fig. 1, Supplementary Tables 1–3 and Supplementary Notes 1 and 2)[24].

To probe the interplay between $EE_{C_{2+}}$ and $SPCE_{C_{2+}}$, we studied CORR in a membrane electrode assembly (MEA) electrolyser under conditions favourable for high $EE_{C_{2+}}$ (ref. 15). The system was equipped with a Cu catalyst on which both cations (K^+; crossing over from the anolyte) and anions (OH^-) promote C–C coupling[2,17]. An increase in the electrolyte alkalinity from a pH of ~8.4 (0.1 KHCO$_3$) to a pH of ~13.0 (0.1 M KOH) and from a pH of ~13.0 (0.1 M KOH) to a pH of ~14.4 (3 M KOH) improved the peak EE of ethylene ($EE_{ethylene}$) and total C_{2+} products (Fig. 1b, Supplementary Figs. 2 and 3 and Supplementary Tables 4–8), in part due to the enhanced proton-coupled electron transfer steps that minimized the cell potential required to achieve peak Faradaic efficiency of C_{2+} products ($FE_{C_{2+}}$) (ref. 18). Any further increase in electrolyte pH (from pH 14.4 (3 M KOH) to pH 14.7 (5 M KOH)) did not yield substantial improvements in the peak $EE_{ethylene}$ and $EE_{C_{2+}}$. However, increasing the electrolyte alkalinity diminished the peak current density of ethylene and C_{2+} products (Supplementary Fig. 2) due to the reduced solubility (and hence limited mass transport) of CO, leading to a sharp decrease in $SPCE_{ethylene}$ and $SPCE_{C_{2+}}$ (Supplementary Fig. 3 and Supplementary Tables 4–8). Increasing the alkalinity from a pH of ~8.4 (0.1 M KHCO$_3$) to a pH of ~13.9 (1 M KOH) and then ~14.7 (5 M KOH) gradually shifted the peak $EE_{ethylene}$ and $EE_{C_{2+}}$ values from a higher current density (>75 mA cm^{-2}) to a low-current-density regime (<50 mA cm^{-2}) (Supplementary Fig. 3). In these current regimes, $SPCE_{ethylene}$ and $SPCE_{C_{2+}}$ peaked at yet lower values (Supplementary Fig. 3), preventing the system from combining higher EE and SPCE combinations simultaneously.

We posited that the performance decays originated partly from the build-up of solvated K^+ within the electrical double layer (EDL) near the negatively charged electrode (a distance of a few nanometres from the outer Helmholtz plane (OHP)), blocking the catalyst surface[25–27] and limiting the mass transport of gaseous reactant. This site-blocking effect would become even more acute with increasing KOH concentration, as it would lead to a further increase in the thickness of the K^+ layer[17]. To test this hypothesis, we added excess K^+ in electrolytes by maintaining a similar pH (pH 13.9 for 1 M KOH and 1 M KOH + 2 M K_2CO_3; and pH 14.7 for 5 M KOH and 5 M KOH + 2 M K_2CO_3) at 50 mA cm^{-2} (Fig. 1c, Supplementary Fig. 4 and Supplementary Tables 9–13). Note that the addition of a carbonate electrolyte did not yield notable changes to the local reaction environment such as the local pH (Supplementary Note 3 and Supplementary Fig. 5) and that all of these electrolytes led to comparable cell voltages in the range of −2.04 to −2.10 V. To minimize any effect that would come from contamination, we used only high-purity precursors, solvents and salts to prepare the electrodes and electrolytes for CORR testing (see Methods). We further excluded the effect of electrolyte impurities (that is, Ni and Fe) through impurity analysis before and after CORR (Supplementary Note 4, Supplementary Fig. 6 and Supplementary Table 14). We found that $EE_{ethylene}$, $EE_{C_{2+}}$, $SPCE_{ethylene}$ and $SPCE_{C_{2+}}$ are diminished with increasing K^+ concentrations, in which the HER begins to dominate (Fig. 1c and Supplementary Tables 9–13).

Theoretical calculations

We then sought to explore, using density functional theory (DFT) calculations, the effect of cations and anions on CORR. We simulated a Cu surface with an OH* coverage ranging from 0–2 (1/9 per site) and a K^+ concentration ranging from 0–3 (1/18 per H_2O molecule), and generated a free energy difference (ΔG) map for CO* reactions to OCCOH* and CHO*—key intermediates along the pathway to C_2 and C_1 products, respectively. DFT calculations confirmed that the increase of OH* coverage favours C–C coupling (lower ΔG) (Fig. 1d, Supplementary Fig. 7 and Supplementary Tables 15 and 16), consistent with the view that high alkalinity promotes C_{2+} products[17]. In contrast, we found volcano-shaped relationships relating K^+ concentration and ΔG, regardless of the OH* coverage. We also calculated the adsorption free energy differences of CO* and H* at various OH* coverages and K^+ concentrations (Supplementary Figs. 8 and 9 and Supplementary Table 17). We found that a low K^+ concentration and a moderate OH* coverage facilitate CO adsorption for CORR over H adsorption for HER. Taken together, these DFT results suggest that limiting K^+ on the catalyst surface provides a route to promote CO adsorption and ensuing reduction towards C–C coupling. They also indicate that—if K^+ accumulation occurs—this must be accompanied by additional OH* to promote C_{2+} products.

Control of ion migration–adsorption

Motivated by the DFT results, we sought to design and implement a catalyst microenvironment that simultaneously controls the transport of anions and cations (that is, maximizes the provision to the catalyst surface of locally generated OH^- while constraining the K^+ concentration at the catalyst surface). In a typical zero-gap, catholyte-free MEA electrolyser, the immediate reaction environment is an EDL, which extends a few nanometres to the bulk catalyst layer. From the bulk to the EDL, solvated cations and anions undergo symmetric migration and adsorption (Fig. 2a,b). In the EDL, the concentration of solvated cations (crossing from the anolyte) builds at the OHP, which depletes both OH^- and CO reactant due to the steric effect[27], as shown by the reaction–diffusion modelling results (Fig. 2c, Supplementary Fig. 10 and Supplementary Notes 3 and 5). This effect is more pronounced at higher current densities and also under low reactant availability due to the K^+ accumulated in the EDL[27], thus diminishing $EE_{C_{2+}}$ and $SPCE_{C_{2+}}$ (Fig. 1b, Supplementary Figs. 2 and 3 and Supplementary Tables 4–13).

To confine the locally generated OH^- and limit the K^+ concentration in the EDL (Fig. 2d,e), we introduced a hydrophobic intermediate layer between the catalyst surface and bulk, with the K^+ diffusion capability lower than that of the bulk catalyst layer. This approach decouples cation and anion transport by enabling an AIM–A and thereby providing abundant CO reactant proximate to the catalyst surface (Fig. 2f, Supplementary Fig. 10 and Supplementary Note 5). With AIM–A, we expected to improve $EE_{C_{2+}}$ and $SPCE_{C_{2+}}$.

COFs for controlled ion transport

We turned our attention to COFs—a class of porous materials formed by covalently linked organic modules—that combine hydrophobic and controlled cation diffusion functionalities, thus extending reactant transport[28–30]. We hypothesized that COFs would create a distinct catalyst microenvironment whereby anion (OH^-) confinement and cation (K^+) migration are allowed through the hydrophobic domains containing ordered porous channels.

Two-dimensional (2D) COFs such as Hex–Aza contain an aromatized π-conjugated system (hydrophobic) associated with a long-range π–π stacking/orbital overlapping (Supplementary Figs. 11–14)[29,31]. They provide a continuous pathway for electron transfer and constrained cation diffusion via cation–π interaction[30–32], enabling reversible cation insertion/extraction capabilities for energy storage devices such as rechargeable batteries. When a 2D COF is coated on a metallic catalyst surface for electrolysis, it forms an AIM–A-mediated EDL in which locally generated OH^- is retained, and the local K^+ concentration is constrained due to the weak cation–π interaction inside the COF layer (Fig. 3a).

Seeking to construct such a CCBH, we dispersed standard Cu nanoparticles and COF in solvents with various weight ratios (wt%) and performed prolonged ultrasonication (see Methods). This enabled COF exfoliation into 2D nanosheets and ensured their homogeneous dispersion. Transmission electron microscopy (TEM) images revealed a homogeneous dispersion of COF over the Cu nanoparticles

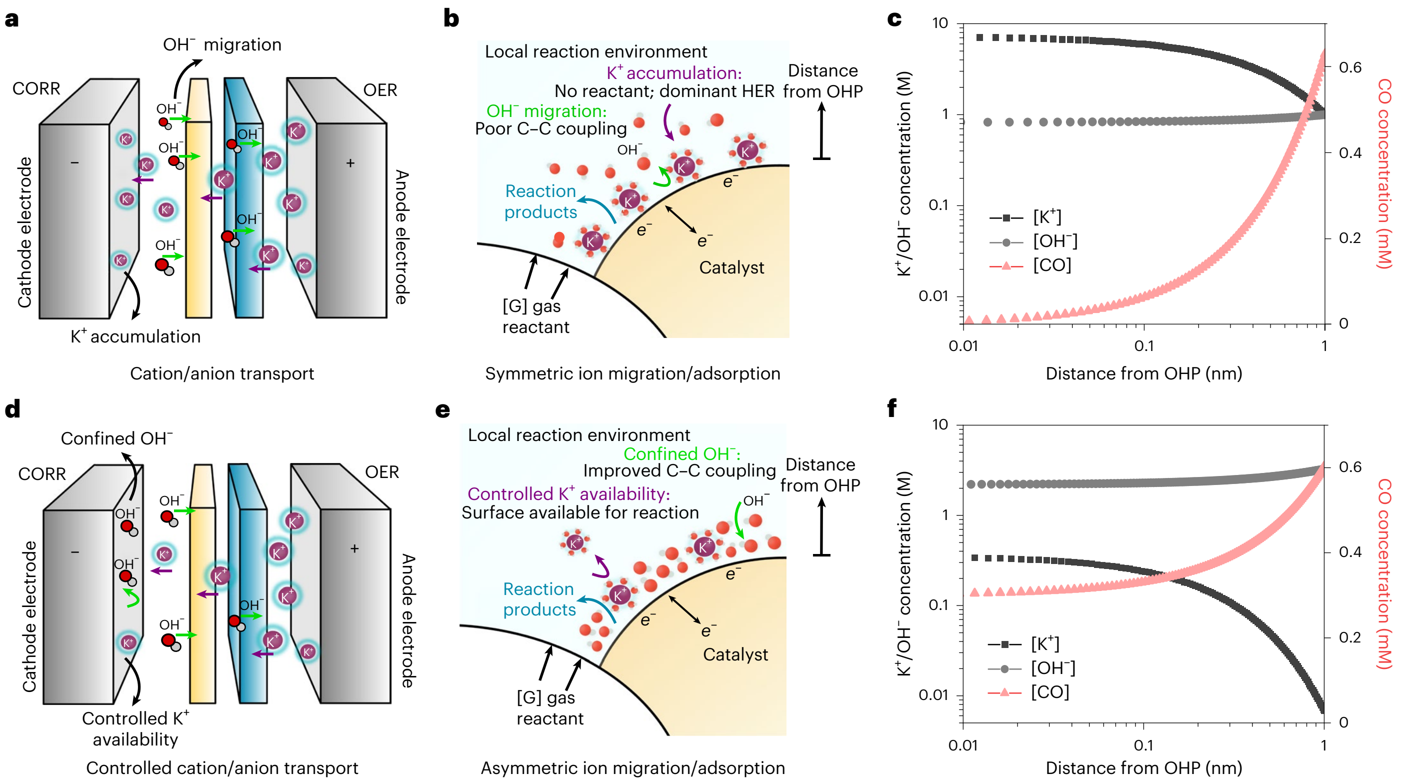

Fig. 2 | Local cation and anion transport in a zero-gap, catholyte-free MEA electrolyser. a, Uncontrolled cation and anion transport in an MEA electrolyser. The schematic shows K$^+$ and OH$^-$ transport, K$^+$ accumulation on the cathode electrode and OH$^-$ migration to the anode electrode. Red represents O atoms, grey represents H atoms and purple represents K atoms. OER denotes the oxygen evolution reaction. **b**, Uncontrolled cation and anion transport in the local reaction environment. The schematic illustrates the accumulation of K$^+$ on the cathode electrode and migration of OH$^-$ to the anode electrode. The K$^+$ accumulation renders the catalyst surface inaccessible to gas phase [G] reactants (CO$_2$ or CO), favouring the HER over CO$_2$RR/CORR. The OH$^-$ migration decreases the local alkalinity, leading to poor C–C coupling and limiting EE$_{C_{2+}}$ and SPCE$_{C_{2+}}$. Atom colours are as in **a**. **c**, K$^+$/OH$^-$ concentration as a function of the distance from the OHP for symmetric ion migration/adsorption. **d**, Controlled cation and anion transport. The schematic shows controlled K$^+$ availability on the cathode electrode and constrained OH$^-$ transport to the anode electrode. Atom colours are as in **a**. OER denotes the oxygen evolution reaction. **e**, Controlled cation and anion transport in the local reaction environment. The schematic illustrates the controlled availability of K$^+$ on the cathode electrode and constrained migration of OH$^-$ to the anode electrode (and hence confined OH$^-$ on the cathode electrode). The controlled K$^+$ availability renders the catalyst surface accessible to gas phase [G] reactant (CO$_2$ or CO), dominating CO$_2$RR/CORR over the HER. The decreased migration of OH$^-$ increases the local alkalinity, leading to improved C–C coupling and an increase in EE$_{C_{2+}}$ and SPCE$_{C_{2+}}$. Atom colours are as in **a**. **f**, K$^+$/OH$^-$ concentration as a function of the distance from the OHP for asymmetric ion migration/adsorption.

(Fig. 3b–e and Supplementary Figs. 15 and 16). We then spray deposited the catalyst ink onto a gas diffusion layer to establish electrodes for performance tests (Supplementary Fig. 17; see Methods). We tuned the hydrophobicity of the CCBH catalyst by varying the COF loading: the static contact angle increased from 115° to 150° with the COF loading altering from 0–25 wt% (Supplementary Fig. 18). Accordingly, the electrochemical roughness factor decreased from 43 to 6 with the COF loading increasing from 0–25 wt% (Supplementary Figs. 19 and 20 and Supplementary Table 18). X-ray diffraction (XRD) patterns and electron microscopy results confirmed that the CCBH catalyst possesses the crystalline characteristics of both Hex–Aza–COF and Cu (Supplementary Fig. 21).

To investigate the AIM–A capability of CCBH catalysts, we performed surface-enhanced Raman spectroscopy (SERS) measurements (Fig. 3f). Ex situ Raman spectrum of COF exhibits strong characteristic signals ranging from 1,100 to 1,800 cm^{-1} and a peak at 610 cm^{-1}, attributable to COF characteristics with the formation of phenazine linkages (C–C=N–C). These COF features become more pronounced during in-situ testing, in which we observed an increasing relative contribution from the 1,470 cm^{-1} band compared with the 1370 cm^{-1} band, attributable to the COF potassisation[30]. This trend is maintained over a range of applied potentials, indicating that the π-conjugated COF backbone with ordered porous channels enables K$^+$ diffusion, consistent with the X-ray photoelectron spectroscopy (XPS) results (Supplementary Fig. 22) and previous studies[30,31].

We then conducted K$^+$ retention measurements on the electrodes of various COF loadings (from 0 to 25 wt%) in 1 M KOH and quantified the local K$^+$ concentration using inductively coupled plasma optical emission spectroscopy[33]. We found that bare Cu shows an order of magnitude higher K$^+$ concentration than CCBH catalyst, regardless of COF loading (Supplementary Fig. 23). When normalized to the electrochemical active surface area (ECSA), we observed an inverse volcano-shaped relationship between local K$^+$ concentration and COF loading (Fig. 3g). Of all the electrodes, bare Cu adsorbs the largest amount of K$^+$ in a wide range of potentials (Supplementary Fig. 24), indicating that the K$^+$ concentration near the active sites can be effectively modulated by varying the COF loading. K$^+$ diffusion measurements also show a similar trend: COF limits the diffusion of K$^+$, leading to a three orders of magnitude lower K$^+$ concentration (Supplementary Note 6 and Supplementary Fig. 25). To deconvolute the role of hydrophobicity, we also performed the K$^+$ retention measurements for the electrodes with similar hydrophobicity (Supplementary Fig. 24). The results show that hydrophobicity is not a major contributor to the K$^+$ retention trends observed.

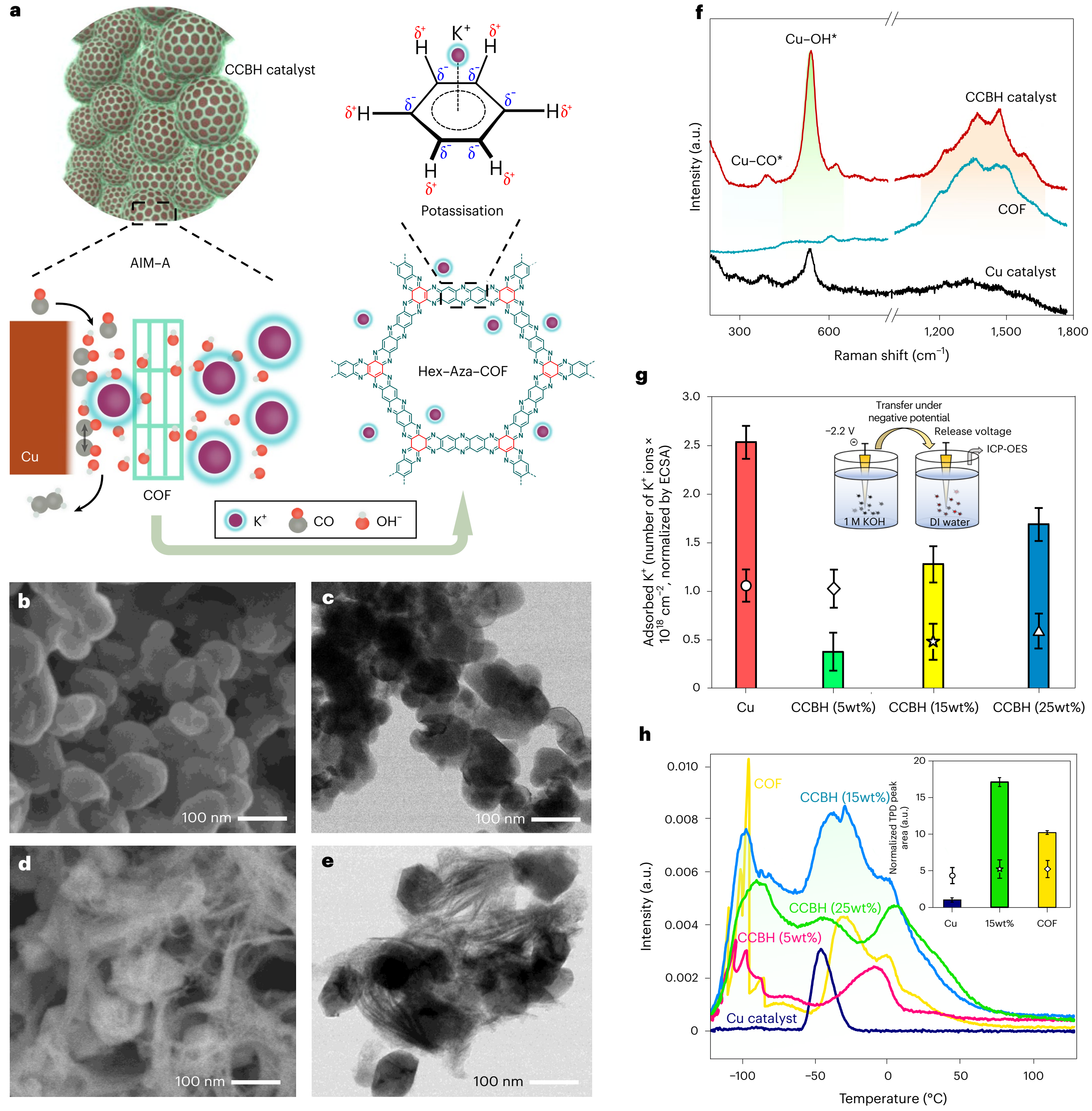

Fig. 3 | The CCBH catalyst. a, Schematic of the CCBH catalyst, illustrating Cu nanoparticles conformably covered by 2D, hydrophobic and π-conjugated Hex–Aza–COF nanosheets[29,31] that exhibit a long-range π–π stacking/orbital overlapping. When coated onto a metallic catalyst surface (CCBH catalyst), COF could provide hydrophobic, continuous pathways for electron transfer and cation diffusion via cation–π interaction[30–32]. As a result, the CCBH catalyst could confine locally generated OH^- and provide good control over the local availability of K^+ ions (due to the weak cation–π interaction). **b**,**c**, SEM (**b**) and TEM (**c**) images of unmodified Cu nanoparticles. **d**,**e**, SEM (**d**) and TEM (**e**) images of the CCBH catalyst with 15 wt% COF loading. The Hex–Aza–COF nanosheets cover the surface of Cu nanoparticles, forming a porous morphology. **f**, Ex situ Raman spectrum of bare Hex–Aza–COF and in situ SERS of the CCBH catalyst with 15 wt% COF loading and Cu nanoparticles at an applied potential of −1.6 V versus Ag/AgCl. **g**, ECSA-normalized adsorbed K^+ concentration on CCBH catalysts of 5, 15 and 25 wt% COF loadings and bare Cu catalyst. The error bars represent the standard deviation of three independent measurements. The data are presented as mean values ± s.d. The inset illustrates the methodology for the K^+ retention measurements (Methods). DI, deionized; ICP-OES, inductively coupled plasma optical emission spectroscopy. **h**, TPD profiles of CO on CCBH catalysts with 5, 15 and 25 wt% COF loadings, bare COF (Hex–Aza–COF) or bare Cu catalyst. The inset presents the normalized TPD peak areas. The error bars represent the standard deviation of two independent measurements. The data are presented as mean values ± s.d.

To characterize the OH^- and CO adsorptions on CCBH catalysts, we focused on the region below 600 cm^{-1} in SERS (Fig. 3f). The bands at 280 and 365 cm^{-1} on bare Cu correspond to adsorbed CO interactions with Cu—the frustrated rotational mode of CO (CO_r) and Cu–CO stretching (CO_s), respectively[34,35]. The band at 530 cm^{-1} is assigned to adsorbed OH^- on Cu[36,37]. Unlike bare Cu, the CCBH catalyst shows an enhanced OH^- adsorption peak. In particular, the CCBH catalyst shows a threefold greater peak intensity ratio of OH^-/CO (I_{OH}–/I_{CO}) compared with bare Cu (Supplementary Figs. 26 and 27). This finding suggests that a hydrophobic COF layer confines OH^- and thereby provides abundant OH^- proximate to the catalyst surface, agreeing with the COMSOL results (Supplementary Fig. 10 and Supplementary Note 5). Additionally, we observed a blue shift of the CO_s band to 390 cm^{-1} on the CCBH catalyst, with the peak CO_r disappeared, suggesting improved CO adsorption[34,37].

To check for the possibility of enhanced CO adsorption on the CCBH catalyst, we performed temperature-programmed desorption (TPD) of CO[38]. First, we conducted a thermal H_2 annealing at 220 °C to remove oxidized Cu species, followed by cooling to −120 °C with CO dosed into the testing chamber. We observed a single TPD peak on bare Cu at −50 °C (Fig. 3h and Supplementary Figs. 28 and 29), corresponding to CO adsorption on regular Cu[38]. In contrast, the CCBH catalyst showed multiple TPD peaks between −120 and 75 °C, due to strong CO adsorption on COF and Cu and at their interfaces. Since the shape and intensity of TPD peaks show diversity depending on the COF loading, we normalized TPD peak areas (Fig. 3h and Supplementary Fig. 29). We found that the CCBH catalyst with a 15 wt% COF loading offered the largest number of CO binding sites, in part due to the abundant Cu/COF interfaces, agreeing with the electrochemical CO stripping results (Supplementary Fig. 30).

Static CO adsorption profiles also show a similar trend (that is, a higher degree of CO uptake on CCBH catalysts) (Supplementary Fig. 31). Taken together, these results support the enhancement of CO adsorption on Cu with COF addition—a result due to constrained K^+ availability and enhanced OH^- at the Cu surface, consistent with the DFT analysis of CO adsorption (Supplementary Fig. 9) and COMSOL results on improved CO concentration at the reaction interface (Supplementary Fig. 10). Enhanced CO adsorption enabled by AIM–A could thus promote CORR.

Investigation of the electroreduction of CO

Next, we evaluated the CORR performance using 1 M KOH at an areal gas flow rate of ~1 sccm cm^{-2}, which was normalized to the geometric electrode area. Bare Cu catalyst showed a peak $SPCE_{C_{2+}}$ of 59% at an $EE_{C_{2+}}$ of 25% and at a C_{2+} current density ($j_{C_{2+}}$) of 137 mA cm^{-2} (Fig. 4a, Supplementary Fig. 32 and Supplementary Table 19). The $SPCE_{C_{2+}}$ on the CCBH catalyst, however, reached 95%, which was achieved at an $EE_{C_{2+}}$ of 41% and a $j_{C_{2+}}$ of 210 mA cm^{-2} (Fig. 4a, Supplementary Fig. 33 and Supplementary Table 20). The CCBH catalyst with AIM–A—by coupling high $EE_{C_{2+}}$ with near-unity $SPCE_{C_{2+}}$ at a wide range of current densities—outcompetes literature benchmark CO_2RR/CORR systems (Fig. 4b and Supplementary Table 21).

The impact of AIM–A on performance was more acute at a higher CO flow rate of ~10 sccm cm^{-2}. The CCBH catalyst achieved a peak $EE_{C_{2+}}$ of >50% (at a $j_{C_{2+}}$ of 88 mA cm^{-2}) and a peak $j_{C_{2+}}$ of 598 mA cm^{-2} (at an $EE_{C_{2+}}$ of 32%) in 1 M KOH (Supplementary Figs. 34 and 35, Supplementary Table 22 and Supplementary Note 7). Tuning of electrode composition/morphology (Supplementary Figs. 17, 36 and 37 and Supplementary Tables 23–27) and electrolyte alkalinity (Supplementary Figs. 38 and 39 and Supplementary Tables 28–30) would enable improvements towards an individual metric under a specific operating condition. With similar performance optimizations, bare Cu showed a peak $EE_{C_{2+}}$ of 37% (at a $j_{C_{2+}}$ of 75 mA cm^{-2}) and a peak $j_{C_{2+}}$ of 367 mA cm^{-2} (at an $EE_{C_{2+}}$ of 23%) (Supplementary Figs. 40 and 41 and Supplementary Tables 31–33).

Noting that hydrophobicity regulates the catalyst microenvironment[39] and enhances gas phase electrolysis[40], we sought to differentiate the performance-enhancing role of AIM–A from hydrophobicity: we designed electrodes of various hydrophobicities through incorporation of hydrophobic polytetrafluoroethylene (PTFE). We prepared catalysts with various PTFE mass loadings (5–50 wt%) and investigated their CORR performance (Supplementary Tables 34–38). The catalyst loaded with 25 wt% PTFE provided hydrophobicity akin to that of the CCBH catalyst (15 wt% COF), as revealed by the contact angle measurements (Supplementary Fig. 18). Accordingly, the catalyst with 25 wt% PTFE yielded the highest performance among the catalysts with various PTFE loadings (Supplementary Tables 34–38). The catalyst with 25 wt% PTFE suppressed the HER, leading to improved $FE_{ethylene}$, $FE_{C_{2+}}$, $EE_{C_{2+}}$ and $SPCE_{C_{2+}}$ compared with bare Cu. The CCBH catalyst suppressed the HER even further, leading to improved $FE_{ethylene}$, $FE_{C_{2+}}$, $EE_{C_{2+}}$ and $SPCE_{C_{2+}}$ compared with both PTFE-based and bare Cu catalysts (Supplementary Figs. 42 and 43 and Supplementary Tables 19, 20 and 36). Overall, the CORR performance of the CCBH catalyst—despite the contribution from hydrophobicity—originates mainly from the AIM–A properties.

We further conducted spectroscopic analysis to examine whether the COF promotes electrolysis by interacting with the Cu catalyst. X-ray absorption spectra (XAS) at the Cu K-edge showed the metallic Cu structure after CORR, although oxidized Cu existed before the reaction due to prolonged ultrasonication and exposure to air during catalyst preparation (Supplementary Fig. 44). The CCBH catalyst possesses a coordination number akin to that of bare Cu (Supplementary Fig. 44). Thus, COF addition does not regulate the oxidation state, nor the coordination number of the Cu in electrolysis. In addition, the N 1*s* XPS results showed the same COF characteristics before and after CORR (Supplementary Fig. 45), indicating that the COF structure does not chemically coordinate with the Cu surface; instead, it modifies the catalyst microenvironment via AIM–A.

With respect to catalyst microenvironment engineering, the COF properties resemble the tandem molecular modification strategies that have contributed positively to the performance of the CO_2RR and CORR systems[8,22,41]. In previous reports, a cation exchange ionomer film was applied to facilitate CO_2/CO transport, whereas an intermediate molecular layer was employed on the Cu catalysts to enhance CO adsorption and its ensuing reduction to C_{2+} products[8,22]. These strategies, however, concentrated stabilizing cations. The accumulation of K^+ on the catalyst restricts the gas reactant diffusion and thereby reduces its utilization in the EDL[27] (Figs. 1c and 2b), limiting $EE_{C_{2+}}$ and $SPCE_{C_{2+}}$ to ~30% (Fig. 1a).

Taking these findings together, we propose in summary a model wherein the COF layer promotes CORR by extending gas transport and confining OH^- to the catalyst microenvironment (akin to previous molecular modification strategies[8,22,41]), and simultaneously (and synergistically) by constraining the K^+ concentration at the catalyst surface. Via AIM–A, one ensures that CO molecules access the active sites and convert to C_{2+} products selectively (enabled by absorbed OH^-), achieving improved $SPCE_{C_{2+}}$ and $EE_{C_{2+}}$. However, excess COF loading limits catalytic active sites, leading to a surplus of local K^+ concentration (Fig. 3g). This excess K^+ diminishes the AIM–A effect, consistent with the volcano-shaped relationship between the ethylene performance and COF loading (Supplementary Fig. 36 and Supplementary Tables 23–27).

The CCBH catalyst is stable, achieving an $EE_{C_{2+}}$ of 40% and a $SPCE_{C_{2+}}$ of 95% for the initial 200 h at 240 mA cm^{-2} (Fig. 4c). Performing impurity analysis under similar operating conditions, we detected no impurity coverage on the CCBH catalyst upon completion of 25 h of continuous operation (Supplementary Note 4, Supplementary Fig. 46 and Supplementary Table 14). The CCBH catalyst is also robust, delivering an average $FE_{C_{2+}}$ of 90% and an average $EE_{C_{2+}}$ of 34% for 150 h at 600 mA cm^{-2} (Supplementary Fig. 47). The CCBH catalyst

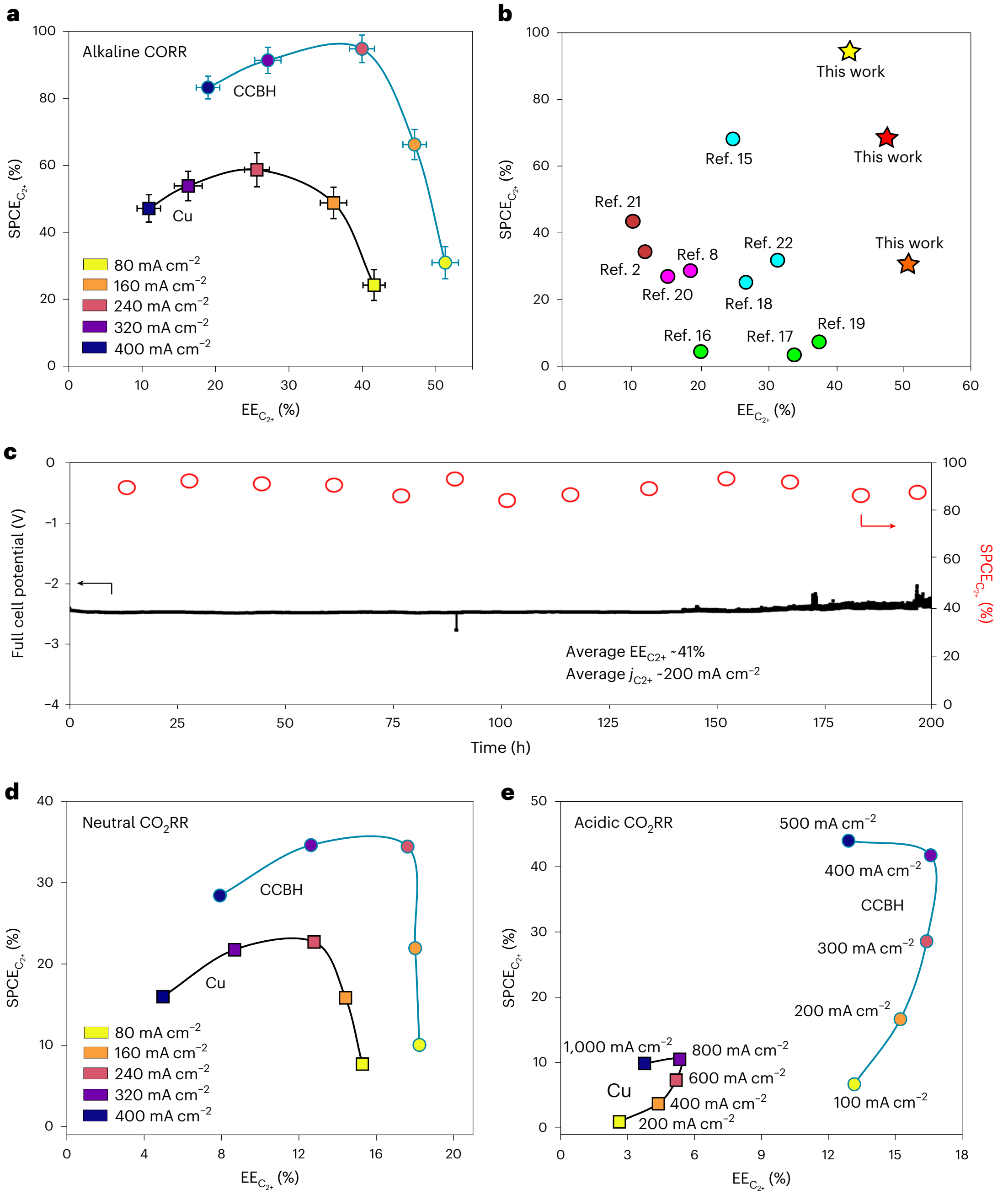

Fig. 4 | The CCBH catalyst for energy- and carbon-efficient CO_2RR/CORR. **a**, CORR-based $SPCE_{C_{2+}}$ versus $EE_{C_{2+}}$ performance of CCBH and bare Cu catalysts. The operating conditions were as follows: anolyte type = 1 M KOH (pH 13.9); anolyte flow rate = 20 ml min^{-1}; average CO inlet flow rate = ~1 sccm cm^{-2}; and cell temperature and pressure under atmospheric conditions. The error bars represent the s.d. of three independent measurements. The data are presented as mean values ± s.d. **b**, Performance assessment of the CCBH catalyst. The CCBH catalyst gives distinct $SPCE_{C_{2+}}$ and $EE_{C_{2+}}$ values (orange star, at 80 mA cm^{-2}; red star, at 160 mA cm^{-2}; yellow star, at 240 mA cm^{-2}), enabling energy- and carbon-efficient electrosynthesis of C_{2+} products from CO. Acidic CO_2RR systems are reported in refs. 2, 21, neutral CO_2RR systems are reported in refs. 8, 20, alkaline CO_2RR systems are reported in refs. 16, 17, 19 and alkaline CORR systems are reported in refs. 15, 18, 22. **c**, Extended CORR performance of the CCBH catalyst at 240 mA cm^{-2}. The CCBH catalyst delivers an average $EE_{C_{2+}}$ of 41%, an average $j_{C_{2+}}$ of ~200 mA cm^{-2} and an $SPCE_{C_{2+}}$ of 91% throughout. The operating conditions were as follows: anolyte type = 1 M KOH (pH 13.9); anolyte flow rate = 20 ml min^{-1}; average CO inlet flow rate = ~1 sccm cm^{-2}; and cell temperature and pressure under atmospheric conditions. **d**, CO_2RR-based $SPCE_{C_{2+}}$ versus $EE_{C_{2+}}$ performance of CCBH and bare Cu catalysts in neutral media. The operating conditions were as follows: anolyte type = 0.1 M $KHCO_3$ (pH 8.4); anolyte flow rate = 20 ml min^{-1}; average CO_2 inlet flow rate = ~1 sccm cm^{-2}; and cell temperature and pressure under atmospheric conditions. **e**, CO_2RR-based $SPCE_{C_{2+}}$ versus $EE_{C_{2+}}$ performance of CCBH and bare Cu catalysts in acidic media. The operating conditions were as follows: catholyte and anolyte type = 1 M H_3PO_4 + 1 M KCl (pH 0.8); catholyte and anolyte flow rate = 20 ml min^{-1}; average CO_2 inlet flow rate = ~1 or ~3.6 sccm cm^{-2} (depending on the current density); and cell temperature and pressure under atmospheric conditions.

maintained its original morphology and structure throughout (Supplementary Figs. 21, 45 and 48). Performing powder XRD and ^{13}C-NMR spectroscopies (Supplementary Figs. 49 and 50), we found that the peaks corresponding to imine −C=N− functionalities remain intact, suggesting that COF in the CCBH catalyst is stable during extended CORR.

Investigation of the electroreduction of CO_2

Noting that K^+ plays a role in CO_2 activation and reduction[2,42], we postulated that the AIM–A concept with constrained K^+ migration may also affect the CO_2RR performance. We compared the CO_2RR performance of the CCBH catalyst with that of bare Cu in various electrolytes. First, we operated in a neutral MEA using 0.1 M $KHCO_3$ (pH 8.4) (Fig. 4d), in which the performance was curtailed by insufficient local CO_2 availability (analogous to the CO diffusion illustrated in Fig. 2b) and CO_2 loss to carbonate formation[2]. At a CO_2 flow rate of ~1 sccm cm^{-2}, bare Cu catalyst showed a peak $SPCE_{C_{2+}}$ of 23% (36% of $SPCE_{CO_2RR}$) at an $EE_{C_{2+}}$ of 13% and a $j_{C_{2+}}$ of 91 mA cm^{-2} (Fig. 4d, Supplementary Fig. 51 and Supplementary Table 40). In contrast, the CCBH catalyst showed better performance, providing a peak $SPCE_{C_{2+}}$ of 32% (47% of $SPCE_{CO_2RR}$), together with an enhanced $EE_{C_{2+}}$ of 18% at a $j_{C_{2+}}$ of 127 mA cm^{-2} (Fig. 4d, Supplementary Fig. 52 and Supplementary Table 41). At a higher CO_2 flow rate of 10 sccm cm^{-2}, the CCBH catalyst achieved an $EE_{C_{2+}}$ of 29% at a $j_{C_{2+}}$ of 457 mA cm^{-2}, whereas bare Cu delivered an $EE_{C_{2+}}$ of 23% at a $j_{C_{2+}}$ of 281 mA cm^{-2} (Supplementary Figs. 53 and 54 and Supplementary Tables 42 and 43). We compared the CO_2RR performance of the CCBH catalyst with that of bare Cu using electrolytes of various K^+ concentrations at a constant pH (Supplementary Fig. 55 and Supplementary Tables 44–48). We found that increasing the K^+ concentration in the electrolyte diminished $EE_{ethylene}$ by promoting hydrogen evolution. This finding signifies that excess K^+ on unmodified Cu catalyst limits CO_2 diffusion and diminishes CO_2RR performance; instead, constraining K^+ via AIM–A leads to enhanced $EE_{C_{2+}}$ and $SPCE_{C_{2+}}$ (Fig. 4d), making it a universal approach that impacts both CO_2 and CO electrolysis.

To further advance $SPCE_{C_{2+}}$ in CO_2RR, we implemented the AIM–A strategy in a slim cell using strong acid electrolytes (at a pH of ~0.8). In such a system, despite the minimized ohmic losses, $EE_{C_{2+}}$ and $SPCE_{C_{2+}}$ are limited by the suboptimal C–C coupling[2]. Specifically, bare Cu suffered from HER, delivering a peak $SPCE_{C_{2+}}$ of 11% (51% of $SPCE_{CO_2RR}$) and an $EE_{C_{2+}}$ of 5% (Fig. 4e, Supplementary Fig. 56 and Supplementary Table 49), consistent with previous studies[2,42,43]. In contrast, the CCBH catalyst—benefitting from the confined CO and OH^- adsorptions—achieved a $SPCE_{C_{2+}}$ of 42% (74% of $SPCE_{CO_2RR}$) and an $EE_{C_{2+}}$ of 17% (Fig. 4e, Supplementary Fig. 57 and Supplementary Table 50). Overall, the CCBH catalyst provided nearly fourfold greater $SPCE_{C_{2+}}$ and $EE_{C_{2+}}$ than bare Cu.

Conclusions

We report a catalyst microenvironment design principle that provides simultaneous control of the transport of cations, anions and gas species, enhancing energy and CO_2/CO conversion and utilization. We present this concept with a CCBH that provides AIM–A. The π-conjugated hydrophobic COFs constrain cation (K^+) diffusion to the catalyst surface while promoting anion (OH^-) and reactant availability at the active sites. By designing and implementing the AIM–A reaction environments, we achieved electrosynthesis of C_{2+} products in a zero-gap system for over 200 h, with a $SPCE_{C_{2+}}$ of 95% and an $EE_{C_{2+}}$ of 41%. This work provides a means to produce valuable chemicals and fuels powered by renewable electricity, with the performance approaching industrial standards.

Methods

Materials and chemicals

All of the chemicals used for COF synthesis, catalyst synthesis, electrode preparation, electrolyte preparation and performance testing, including 2,3,6,7-tetraamino-phenazine hydrochloride, hexaketocyclohexane octahydrate (97%), ethylene glycol (anhydrous; 99.8%), acetic acid (>99%), methanol (anhydrous; 99.8%), 2-propanol (anhydrous; 99.5%), potassium chloride (American Chemical Society (ACS) reagent; 99.0–100%), phosphoric acid (85 vol%), potassium phosphate monobasic (ACS reagent; >99.0), potassium sulfate (ACS reagent; >99.0% powder), potassium iodide (ACS reagent; >99%), potassium hydroxide (pellets; 99.99%), perchloric acid (ACS reagent; 70 vol%), hydrochloric acid (ACS reagent; 37 vol%), Aquivion (D79-25BS; 25 wt% in water; perfluorosulfonic acid equivalent weight: 790 g mol^{-1} SO_3H; contains CF_3 polymer chain ends as a stabilizer), Cu nanopowder (25 nm particle size (TEM); 99.5%), dimethyl sulfoxide (anhydrous; >99.9%) and deuterium oxide (99.9%), were from Sigma–Aldrich. Deionized water (18.2 MΩ) was used for the preparation of COF-modified Cu nanoparticles. Fumasep (FAA-3-50) and Nafion (XL) membranes, hydrophobic carbon paper (22 BB; Sigracet) and titanium fibre felt (60–70% porosity and 2 mm thickness) were from the Fuel Cell Store. The MEA electrolyser (5 cm^2) and Sustainion X37-50 membrane were from Dioxide Materials. The PTFE with a pore size of 450 nm was from Beijing Zhongxingweiye Instrument. Cu was sputtered onto the PTFE substrate under a vacuum (~10^{-6} Torr) using a Cu target (>99.99%) in an Angstrom Nexdep sputtering system. A constant sputtering rate of 0.8 Å s^{-1} was applied until a catalyst thickness of 200 nm was achieved.

Synthesis of the COF

The synthesis of Hex–Aza–COF was performed via the solvothermal condensation reaction[31]. The solvothermal condensation reaction occurred between hexaketocyclohexane octahydrate and 2,3,6,7-tetraamino-phenazine hydrochloride in a solvent containing ethylene glycol and 3.0 M acetic acid (with a volumetric ratio of 1:1). The reactants and solvents were transferred to a screw-capped Pyrex tube (20 ml) and sonicated for 15 min under nitrogen. Upon sonication, the Pyrex tubes were placed inside a pre-heated oven and incubated for 4 h at 65 °C. The temperature was gradually increased to 120–150 °C and the reaction continued for 4 d. The Hex–Aza–COF powders were isolated by filtration, washed with a solvent containing acetone and deionized water and dried under vacuum.

COF-modified copper catalyst

The Cu nanoparticles were modified by Hex–Aza–COF through ultrasonication. The Cu nanoparticles and Hex–Aza–COF powder were physically mixed in a solvent containing methanol and deionized water (with a volumetric ratio of 1:1). The weight ratio (wt%) between Hex–Aza–COF and the Cu nanoparticles was varied from 5–25%. The resulting ink was sonicated in an ultrasonic bath for 12 h at 45 °C. The resulting ink was used in the catalyst ink.

Preparation of gas diffusion electrodes

The gas diffusion electrodes (GDEs) for CORR were prepared by spray depositing a homogeneous catalyst ink onto a carbon paper substrate. The substrates used for the acidic media CO_2RR experiments were based on Cu sputtered onto a PTFE substrate (Cu/PTFE). The catalyst thickness was 200 nm. A sputtering rate of 0.80 Å s^{-1} was used at 10^{-6} Torr. For an electrode geometric area of 5 cm^2, the catalyst ink was prepared by adding 15 mg of a polymeric binder (D79-25BS) to the ink containing 15 mg Hex–Aza–COF and 100 mg Cu nanoparticles (25 nm particle size (TEM); 99.5%) and sonicating the resulting ink for 2 h in an ultrasonic bath. The resulting ink was spray deposited onto a substrate (hydrophobic carbon paper for the MEA and Cu/PTFE for the acidic media flow cell) until a catalyst loading of 0.8 mg cm^{-2} was achieved. An excess of catalyst ink was prepared considering the loss of materials during the spray deposition. The nominal catalyst loading of 0.8 mg cm^{-2} was ensured. The resulting electrode was dried under vacuum for 12 h before performance testing. The control electrodes were prepared following the same recipe without adding COF—namely, the catalyst ink was composed of 100 mg Cu nanoparticles (25 nm particle size (TEM); 99.5%) and 15 mg of a polymeric binder (D79-25BS).

Materials characterization

Scanning electron microscopy (SEM) imaging was performed via a high-resolution scanning electron microscope (S-5200; Hitachi). XPS measurements were performed with a PHI 5700 electron spectroscopy for chemical analysis system, which uses Al Kα X-ray diffraction as the energy source for excitation. TEM imaging and energy dispersive X-ray (EDX) elemental mapping were performed via a field emission transmission electron microscope (HF3300; Hitachi). Structural characteristics of the electrodes were analysed by XRD at room temperature on a MiniFlex 600 instrument with a Cu target ($\lambda = 1.54056$ Å).

XAS measurements were performed at beamline 20-BM of the Advanced Photon Source at Argonne National Laboratory. XAS data were analysed using the Athena and Artemis software included in a standard IFEFFIT package. Raman spectra were recorded using a Renishaw Raman spectrometer and analysed and averaged using WiRE 4.4 software. Each Raman spectrum presented in this work was an average of over ten scans. The setup contained a 785 nm excitation laser and 1,200 mm^{-1} grating. The laser power was 200 µW and a 63× magnification immersion objective was used. The custom-made, three-electrode Raman cell had a 1 cm × 1 cm electrolyte reservoir, in which the immersion objective was immersed. The reservoir was separated from the gas chamber via a GDE. A Pt wire was used as the counter electrode and Ag/AgCl was used as the reference electrode. The CO flow rate was ~1 sccm cm^{-2}. 1 M KOH was used as the electrolyte.

Static contact angle measurements were performed via the sessile drop method on a video-based measurement system. The measurements were performed by: (1) placing a droplet of water onto a circular-shaped specimen extracted from a GDE of interest; (2) fitting a tangent line to the intersection of the solid, liquid and gas phases using software; and (3) determining the external angle using software.

K^+ retention measurements were carried out in 1 M KOH using a two-electrode configuration in a beaker. The measurements were performed by following a procedure similar to that described in ref. 33. A Pt electrode was used as the counter electrode and a GDE with a catalyst of interest (with a geometric area of 1 cm × 1.5 cm) was used as the working electrode. The back side of the GDE was fully covered with a Kapton type. Constant full cell potentials of −1.9, −2.2 and −2.5 V were applied immediately before immersing the GDE into 1 M KOH. The GDE was taken out of the solution after 120 s and transferred to a vial with 10 ml deionized water before releasing the applied potential. Then, any absorbed K^+ on the GDE was released into the deionized water. The amount of K^+ in the water was detected using an inductively coupled plasma optical emission spectrometer detector (Agilent Dual View 720 with a charge-coupled device) that enabled coverage of the full wavelength (167 and 785 nm). The K^+ concentration was normalized by ECSA.

K^+ diffusion measurements were performed in a two-electrode configuration following a procedure similar to that reported in ref. 44. Pure water was circulated through the cathode chamber and 1 M KOH was circulated through the anode chamber (Supplementary Fig. 25). Both chambers (1 cm × 1 cm) were physically separated by a membrane with and without a COF layer. The CORR was initiated by applying a constant potential of −2.2 V, and the K^+ concentration in the catholyte and the corresponding current were monitored.

ECSA measurements were performed in a custom-made, three-electrode flow cell. A GDE (1 cm × 1 cm) was used as the working electrode, with a nickel foam as the counter electrode and Ag/AgCl as the reference electrode. Both anolyte and catholyte were 1 M KOH. Cyclic voltammograms were performed between −0.15 and −0.25 V versus Ag/AgCl at 40, 60, 80, 100 and 120 mV s^{-1} (Supplementary Fig. 19). The capacitance for each catalyst was obtained experimentally. A reference surface factor of 1 for Cu foil was utilized to calculate the surface roughness factor[1].

TPD measurements were performed by following a procedure similar to that reported in ref. 38 and using an AutoChem 2920 Automated Catalyst Characterization System. COF-modified Cu nanoparticles and control catalyst (Cu nanoparticles) with a loading of 500 mg were loaded onto U-shaped quartz sample tubes. The sample tube containing the catalyst was then connected to a gas line with a temperature controller. The catalysts were pretreated with a hydrogen flow of 50 ml min^{-1} at 220 °C for 2 h to remove any surface contaminants and reduce any surface oxides. The catalyst was then exposed to a helium gas flow for 1 h to remove any gas contaminants in the line and on the catalyst surface. For the TPD measurements, the catalyst samples were cooled down to −120 °C using a liquid nitrogen cryocooler setup. CO gas (10% CO/He) was then purged for an additional 1 h to the sample tube to remove any potential physisorbed CO gas. Catalysts with chemisorbed CO gas were subjected to temperature-programmed heating from −120 to 130 °C. The desorbed chemisorbed CO gas coming out from the catalyst during the heating was monitored using a thermal conductivity detector and an attached mass spectrometer. The CO TPD peak areas were normalized with the lowest peak area, which was the area obtained for Cu nanoparticles.

Static CO adsorption measurements were performed on a 3Flex Surface Characterization Analyzer with enhanced corrosion resistance from Micromeritics. The cryogenic temperatures during adsorption measurements were controlled using liquid nitrogen baths at 77 K. The ambient temperature was controlled using a thermostat bath at 298 K. CO adsorption measurements were performed in a ventilated enclosure to avoid any exposure to CO. Appropriate sensors from STANDGAS were used to detect any possible CO leakage.

Solid-state NMR spectroscopy (^{13}C-NMR) measurements were performed on Bruker Avance III spectrometers at a resonance frequency of 600 MHz. The experiments were performed using a conventional double-resonance 3.2 mm Cross-Polarization/Magic-Angle Spinning (CP/MAS) probe. The external references tetramethylsilane and adamantane were used for reporting NMR chemical shifts.

CO_2RR performance in acidic media

Acidic CO_2RR experiments were carried out in a slim flow cell using a two-electrode configuration. The setup was composed of an catholyte chamber, an anolyte chamber and a gas flow chamber. The electrode geometric area was 1 cm^2. The catholyte chamber was physically separated from the gas chamber via a cathode electrode, with the catalyst side facing the catholyte and the substrate side facing the gas chamber. IrOx/Ti was employed as the anode catalyst. The IrOx/Ti electrodes were prepared by: etching the Ti fibre felts in 6 M HCl at 75 °C for 30 min; rinsing the etched Ti felts with deionized water for 40 min; immersing the Ti felts into an ink of 2-propanol, iridium(IV) chloride dehydrate (Premion; 99.99%) and HCl and drying at 100 °C for 10 min; and sintering at 500 °C for 10 min. A total Ir loading was 1 mg cm^{-2}. A cation exchange membrane (Nafion XL) was used to separate the anolyte and catholyte chambers. Catholyte and anolyte were fed into their respective chambers through silicon tubing at 15 ml min^{-1}. Peristaltic pumps were responsible for the supply of electrolytes. Anolyte and catholyte entered the chambers from the bottom and exited from the top, forming a close cycle. A digital mass flow controller (SmartTrack 100; Sierra) was employed to supply CO_2 with a constant flow rate to the gas chamber. The CO_2 gas cylinder was purchased from Linde Gas. All of the electrochemical measurements were performed using an electrochemical workstation (Autolab PGSTAT302N) equipped with a current booster (Metrohm Autolab; 10 A). The catholytes and anolytes with a pH of ~0.80 were prepared using 1 M phosphoric acid (H_3PO_4) as the base electrolyte, with incorporation of 1 M potassium chloride (KCl). The CO_2RR performance was investigated under galvanostatic mode. 1 M H_3PO_4 was used as the anolyte and 1 M H_3PO_4 and 1 M KCl were used as the catholyte. COF-modified Cu nanoparticle-deposited Cu/PTFE electrodes were used as the cathode electrodes, while Cu nanoparticle-deposited Cu/PTFE electrodes were used as the control electrodes.

The CO_2RR was initiated by applying a constant current density of −0.1 A cm^{-2} and the CO_2RR products were collected from the cathodic gas and liquid streams. The gas products were collected in 1 ml volumes using gas-tight syringes (Hamilton chromatography syringes) and injected into a gas chromatograph (Clarus 680; PerkinElmer). The gas chromatograph was equipped with a thermal conductivity detector for the simultaneous detection of hydrogen, oxygen, carbon monoxide and nitrogen signals, as well as a flame ionization detector for the detection of methane and ethylene. The gas chromatograph was equipped with packed columns of Molecular Sieve 5A and Carboxen-1000. Argon (Linde; 99.999%) was used as the carrier gas.

CO_2RR/CORR performance in neutral and alkaline media

The CO_2RR/CORR performance analyses were investigated in an MEA electrolyser using neutral and alkaline anolytes. The experiments were carried out using an electrochemical test station. The test station was equipped with a potentiostat, a current booster (Metrohm Autolab; 10 A), a commercial CO_2RR MEA electrolyser (Dioxide Materials), a mass flow controller (SmartTrak 100; Sierra), an anolyte container, a humidifier and a peristaltic pump with silicon tubing. The CO_2RR MEA electrolyser was composed of a titanium anode and stainless steel cathode flow-field plates. The geometric areas were 5 cm^2. The MEA was composed of a cathode electrode (COF-modified Cu nanoparticles or Cu nanoparticles supported on carbon paper), an anode electrode (IrOx/Ni) and an anion exchange membrane (Fumasep FAA-3-50 for CORR and Sustainion X37-50 for CO_2RR). The electrodes were placed on their respective plates and then separated by an AEM. The assembly was made applying an equal compression torque to the bolts. The AEM was rinsed with deionized water for 10 min before assembly. The anode flow field was responsible for supplying the anolyte, whereas the cathode flow field was responsible for supplying humidified CO or CO_2. The IrOx/Ni electrodes were prepared by: (1) immersing the Ti felts into an ink of 2-propanol, iridium(IV) chloride dehydrate (Premion; 99.99%) and HCl; (2) drying at 100 °C for 10 min; and (3) sintering at 500 °C for 10 min. The Ir mass loading was 1 mg cm^{-2}. Then, anolyte (KOH for CORR and $KHCO_3$ for CO_2RR) was supplied to the anode chamber and fully humidified reactant (CO for CORR and CO_2 for CO_2RR) was supplied to the cathode with a constant flow rate. Unless otherwise stated, the reactant flow rates were either ~10 or ~1 sccm cm^{-2}. A current density of 100 mA cm^{-2} was applied and then the current density was increased with 100 mA cm^{-2} increments upon voltage stabilization and product collection, which typically took 25–30 min. The gas products were collected in 1 ml volumes three times with frequent time intervals, and into the gas chromatograph for product quantification. The liquid products were collected from both the anode and cathode liquid streams.

CO_2RR/CORR product analysis

The gas chromatography spectra for each gas injection—with the current density, CO_2 outlet flow rate and fraction of gas products—was used to evaluate the CO_2RR performance as follows:

$$\text{Faradaic efficiency } (\%) = N \times F \times \upsilon \times r / (i \times V_m)$$

where N represents the number of electrons transferred, F represents the Faradaic constant, υ represents the gas flow rate, r represents the concentration of the product of interest in ppm, i represents the total current and V_m represents the unit molar volume of product of interest. The flow rate at the cathode outlet was measured using a bubble flow meter. The liquid products were characterized via ^{1}H NMR spectroscopy (Agilent DD2 600 MHz NMR Spectrometer) with water peak suppression. Dimethyl sulfoxide and deuterium oxide were used as the reference standard and lock solvent, respectively. The NMR spectra for each condition—with the amount of charge passing and the duration of the reaction—were used to quantify the FE towards liquid CO_2RR products using:

$$\text{Faradaic efficiency } (\%) = N \times F \times n_{\text{product}} / Q$$

where n_{product} represents the total number of moles of product and $Q = i \times t$ represents the total charge passing during measurement.

EE calculation

The full cell EEs were calculated using:

$$\text{EE}_{\text{product}} = \frac{E^{\text{o}}_{\text{cell}}}{E_{\text{cell}}} \times \text{FE}_{\text{product}} \times 100\%$$

$$E^{\text{o}}_{\text{cell}} = \frac{\Delta G^{\text{o}}}{-zF}$$

where $E^{\text{o}}_{\text{cell}}$ represents the thermodynamic cell potential for products ($E^{\text{o}}_{\text{ethylene}} = 0.17$ V, ethylene $E^{\text{o}}_{\text{cell}} = 1.06$ V; $E^{\text{o}}_{\text{ethanol}} = 0.19$ V, ethanol $E^{\text{o}}_{\text{cell}} = 1.04$ V; $E^{\text{o}}_{\text{propanol}} = 0.2$ V, propanol $E^{\text{o}}_{\text{cell}} = 1.03$ V; $E^{\text{o}}_{\text{acetate}} = 0.45$ V and acetate $E^{\text{o}}_{\text{cell}} = 0.78$ V), ΔG^{o} represents the change in Gibbs free energy for the reaction and E_{cell} represents the applied cell voltage (non-iR compensated).

SPCE calculation

SPCE towards gas, liquid or a group of gas and liquid products at 25 °C and 1 atm was calculated using the following equation:

$$\text{SPCE} = (j \times 60\text{ s}) / (N \times F) \div \left(\text{flow rate}\left(\text{l min}^{-1}\right) \times 1\,(\text{min})\right) / \left(24.05\ \left(\text{l mol}^{-1}\right)\right)$$

where j represents the partial current density towards a single product or a group of products and N represents the number of electrons transferred to form 1 mole of target product.

DFT calculations

We performed all spin-unrestricted DFT calculations by using the Vienna Ab initio Simulation Package[45,46]. We constructed the plane waves using the projector augmented-wave method with a cut-off energy of 400 eV[47,48]. The exchange–correlation energy was determined using the Perdew–Burke–Ernzerhof formulation of the generalized gradient approximation[49]. Here a (3 × 3 × 4) Cu(111) model was used to simulate the Cu surface. To fully consider the solvation effect, 18 explicit water molecules were optimized and a local minimum via the hydrogen bond network was formed. Each slab was separated from its periodic images in the z axis by ~15 Å of vacuum space. The bottom two atomic layers were fixed to simulate the bulk structure. The two top layers were allowed to relax. The Brillouin zone integrations were performed on a Monkhorst–Pack 6 × 6 × 1 k-point mesh[50]. The self-consistent energy convergence criterion was 10^{-5} eV and the force convergence for geometry optimization was 0.05 eV Å^{-1}. The model considered zero, one or two OH* groups on a Cu(3 × 3) periodic surface. Possible adsorption configurations were tested to find the most stable structures when CO adsorbed on the Cu surface with different OH* coverage. Meanwhile, zero, one, two or three potassium atoms were incorporated into water layers to simulate different potassium concentrations. Two competing reaction pathways of CORR were considered as follows.

$$\text{CO}^* + \text{H}^+ + e^- \rightarrow \text{CHO}^*$$

$$\text{CO}^* + \text{CO}^* + \text{H}^+ + e^- \rightarrow \text{OCCOH}^*$$

The competition of CO* and H* at various K$^+$ concentrations and OH* coverages was also calculated to explore the effect of environmental conditions on CO coverage and the HER on the surface of the Cu catalyst. Herein, the differences in Gibbs free energies for CO* protonation, C–C coupling, CO adsorption and H adsorption were obtained by the correction of Gibbs free energy (G) using:

$$G = E + \text{ZPE} + \int C p dT - TS$$

where E represents the DFT-calculated energy, ZPE represents the zero-point energy, C_p represents the heat capacity, S represents the entropy and T represents the room temperature (298.15 K).

COMSOL modelling

The local concentrations of K^+, OH^- and CO at the catalyst layer with or without COF were modelled in COMSOL (COMSOL Multiphysics version 5.5) using a 1D reaction–diffusion model. The Secondary Current Distribution and Transport of Diluted Species physics modules within COMSOL were used to model the interactions between K^+, H^+, OH^-, CO and H_2O in a time-dependent study. Details are included in Supplementary Note 3.

Data availability

All of the data supporting the findings of this study are available within the published article and its Supplementary Information files. Source data are provided with this paper.

References

1. Li, C. W., Ciston, J. & Kanan, M. W. Electroreduction of carbon monoxide to liquid fuel on oxide-derived nanocrystalline copper. *Nature* **508**, 504–507 (2014).
2. Huang, J. E. et al. CO_2 electrolysis to multicarbon products in strong acid. *Science* **372**, 1074–1078 (2021).
3. Nitopi, S. et al. Progress and perspectives of electrochemical CO_2 reduction on copper in aqueous electrolyte. *Chem. Rev.* **119**, 7610–7672 (2019).
4. Jouny, M., Hutchings, G. S. & Jiao, F. Carbon monoxide electroreduction as an emerging platform for carbon utilization. *Nat. Catal.* **2**, 1062–1070 (2019).
5. De Luna, P. et al. What would it take for renewably powered electrosynthesis to displace petrochemical processes? *Science* **364**, eaav3506 (2019).
6. Li, J. et al. Enhanced multi-carbon alcohol electroproduction from CO via modulated hydrogen adsorption. *Nat. Commun.* **11**, 3685 (2020).
7. Wang, X. et al. Efficient electrically powered CO_2-to-ethanol via suppression of deoxygenation. *Nat. Energy* **5**, 478–486 (2020).
8. Ozden, A. et al. High-rate and efficient ethylene electrosynthesis using a catalyst/promoter/transport layer. *ACS Energy Lett.* **5**, 2811–2818 (2020).
9. Shin, H., Hansen, K. U. & Jiao, F. Techno-economic assessment of low-temperature carbon dioxide electrolysis. *Nat. Sustain.* **4**, 911–919 (2021).
10. Chen, C., Li, Y. & Yang, P. Address the “alkalinity problem” in CO_2 electrolysis with catalyst design and translation. *Joule* **5**, 737–742 (2021).
11. Rabinowitz, J. A. & Kanan, M. W. The future of low-temperature carbon dioxide electrolysis depends on solving one basic problem. *Nat. Commun.* **11**, 5231 (2020).
12. Ren, S. et al. Molecular electrocatalysts can mediate fast, selective CO_2 reduction in a flow cell. *Science* **365**, 367–369 (2019).
13. Kim, D. et al. Selective CO_2 electrocatalysis at the pseudocapacitive nanoparticle/ordered-ligand interlayer. *Nat. Energy* **5**, 1032–1042 (2020).
14. Li, J. et al. Efficient electrocatalytic CO_2 reduction on a three-phase interface. *Nat. Catal.* **1**, 592–600 (2018).
15. Ripatti, D. S., Veltman, T. R. & Kanan, M. W. Carbon monoxide gas diffusion electrolysis that produces concentrated C_2 products with high single-pass conversion. *Joule* **3**, 240–256 (2019).
16. De Arquer, P. F. et al. CO_2 electrolysis to multicarbon products at activities greater than 1 A cm^{-2}. *Science* **367**, 661–666 (2020).
17. Dinh, C. T. et al. CO_2 electroreduction to ethylene via hydroxide-mediated copper catalysis at an abrupt interface. *Science* **360**, 783–787 (2018).
18. Jouny, M., Luc, W. & Jiao, F. High-rate electroreduction of carbon monoxide to multi-carbon products. *Nat. Catal.* **1**, 748–755 (2018).
19. Ma, W. et al. Electrocatalytic reduction of CO_2 to ethylene and ethanol through hydrogen-assisted C–C coupling over fluorine-modified copper. *Nat. Catal.* **3**, 478–487 (2020).
20. Gabardo, C. M. et al. Continuous carbon dioxide electroreduction to concentrated multi-carbon products using a membrane electrode assembly. *Joule* **3**, 2777–2791 (2019).
21. O’Brien, C. P. et al. Single pass CO_2 conversion exceeding 85% in the electrosynthesis of multicarbon products via local CO_2 regeneration. *ACS Energy Lett.* **6**, 2952–2959 (2021).
22. Ozden, A. et al. Cascade CO_2 electroreduction enables efficient carbonate-free production of ethylene. *Joule* **5**, 706–719 (2021).
23. Ozden, A. et al. Carbon-efficient carbon dioxide electrolysers. *Nat. Sustain.* **5**, 563–573 (2022).
24. Sisler, J. et al. Ethylene electrosynthesis: a comparative techno-economic analysis of alkaline vs membrane electrode assembly vs CO_2–CO–C_2H_4 tandems. *ACS Energy Lett.* **6**, 997–1002 (2021).
25. Xu, Y. et al. Self-cleaning CO_2 reduction systems: unsteady electrochemical forcing enables stability. *ACS Energy Lett.* **6**, 809–815 (2021).
26. Endrődi, B. et al. Operando cathode activation with alkali metal cations for high current density operation of water-fed zero-gap carbon dioxide electrolysers. *Nat. Energy* **6**, 439–448 (2021).
27. Bohra, D., Chaudhry, J. H., Burdyny, T., Pidko, E. A. & Smith, W. A. Modeling the electrical double layer to understand the reaction environment in a CO_2 electrocatalytic system. *Energy Environ. Sci.* **12**, 3380–3389 (2019).
28. Lin, S. et al. Covalent organic frameworks comprising cobalt porphyrins for catalytic CO_2 reduction in water. *Science* **349**, 1208–1213 (2015).
29. Kandambeth, S., Kale, V. S., Shekhah, O., Alshareef, H. N. & Eddaoudi, M. 2D covalent-organic framework electrodes for supercapacitors and rechargeable metal-ion batteries. *Adv. Energy Mater.* **12**, 2100177 (2022).
30. Chen, X., Zhang, H., Ci, C., Sun, W. & Wang, Y. Few-layered boronic ester based covalent organic frameworks/carbon nanotube composites for high-performance K-organic batteries. *ACS Nano* **13**, 3600–3607 (2019).
31. Kandambeth, S. et al. Covalent organic frameworks as negative electrodes for high-performance asymmetric supercapacitors. *Adv. Energy Mater.* **10**, 2001673 (2020).
32. Ma, J. C. & Dougherty, D. A. The cation–π interaction. *Chem. Rev.* **97**, 1303–1324 (1997).
33. Liu, M. et al. Enhanced electrocatalytic CO_2 reduction via field-induced reagent concentration. *Nature* **537**, 382–386 (2016).
34. Zhan, C. et al. Revealing the CO coverage-driven C–C coupling mechanism for electrochemical CO_2 reduction on Cu_2O nanocubes via operando Raman spectroscopy. *ACS Catal.* **11**, 7694–7701 (2021).
35. Hoang, T. T. H. et al. Nanoporous copper–silver alloys by additive-controlled electrodeposition for the selective electroreduction of CO_2 to ethylene and ethanol. *J. Am. Chem. Soc.* **140**, 5791–5797 (2018).
36. Niaura, G. Surface-enhanced Raman spectroscopic observation of two kinds of adsorbed OH^- ions at copper electrode. *Electrochim. Acta* **45**, 3507–3519 (2000).
37. Zhao, Y. et al. Speciation of Cu surfaces during the electrochemical CO reduction reaction. *J. Am. Chem. Soc.* **142**, 9735–9743 (2020).
38. Verdaguer-Casadevall, A. et al. Probing the active surface sites for CO reduction on oxide-derived copper electrocatalysts. *J. Am. Chem. Soc.* **137**, 9808–9811 (2015).

39. Wakerley, D. et al. Bio-inspired hydrophobicity promotes CO_2 reduction on a Cu surface. *Nat. Mater.* **18**, 1222–1227 (2019).
40. Xing, Z., Hu, L., Ripatti, D. S., Hu, X. & Feng, X. Enhancing carbon dioxide gas-diffusion electrolysis by creating a hydrophobic catalyst microenvironment. *Nat. Commun.* **12**, 136 (2021).
41. Kim, C. et al. Tailored catalyst microenvironments for CO_2 electroreduction to multicarbon products on copper using bilayer ionomer coatings. *Nat. Energy* **6**, 1026–1034 (2021).
42. Monteiro, M. C. O. et al. Absence of CO_2 electroreduction on copper, gold and silver electrodes without metal cations in solution. *Nat. Catal.* **4**, 654–662 (2021).
43. Bondue, C. J., Graf, M., Goyal, A. & Koper, M. T. M. Suppression of hydrogen evolution in acidic electrolytes by electrochemical CO_2 reduction. *J. Am. Chem. Soc.* **143**, 279–285 (2021).
44. Rubcumintara, T. & Han, K. N. Metal ionic diffusivity: measurement and application. *Miner. Process. Extr. Metall. Rev.* **7**, 23–47 (2007).
45. Kresse, G. & Hafner, J. Ab initio molecular dynamics for liquid metals. *Phys. Rev. B* **47**, 558–561 (1993).
46. Kresse, G. & Furthmüller, J. Efficient iterative schemes for ab initio total-energy calculations using a plane-wave basis set. *Phys. Rev. B* **54**, 11169–11186 (1996).
47. Blöchl, P. E., Jepsen, O. & Andersen, O. K. Improved tetrahedron method for Brillouin-zone integrations. *Phys. Rev. B* **49**, 16223–16233 (1994).
48. Kresse, G. & Joubert, D. From ultrasoft pseudopotentials to the projector augmented-wave method. *Phys. Rev. B* **59**, 1758–1775 (1999).
49. Perdew, J. P., Burke, K. & Ernzerhof, M. Generalized gradient approximation made simple. *Phys. Rev. Lett.* **77**, 3865–3868 (1996).
50. Monkhorst, H. J. & Pack, J. D. Special points for Brillouin-zone integrations. *Phys. Rev. B* **13**, 5188–5192 (1976).

Acknowledgements

This work was financially supported by the Ontario Research Fund – Research Excellence programme, the Natural Sciences and Engineering Research Council (NSERC) of Canada and Natural Resources Canada's Clean Growth Program. This research used synchrotron resources of the Advanced Photon Source (an Office of Science User Facility operated for the US Department of Energy (DOE) Office of Science by Argonne National Laboratory) and was supported by the US DOE under contract number DE-AC02-06CH11357, as well as the Canadian Light Source and its funding partners. Support from the Canada Research Chairs Program is gratefully acknowledged, as is support from an NSERC E.W.R. Steacie Fellowship to D.S. J.L. thanks the National Natural Science Foundation of China (grant number BE3250011), the National Key Research and Development Program of China (grant number 2022YFA1505100), and Shanghai Jiao Tong University (grant number WH220432516) for support. F.P.G.d.A. acknowledges funding from CEX2019-000910-S (MCIN/AEI/10.13039/501100011033), Fundación Cellex, Fundació Mir-Puig, Generalitat de Catalunya through CERCA and the La Caixa Foundation (100010434; EU Horizon 2020 Marie Skłodowska-Curie grant agreement 847648).

Author contributions

D.S., E.H.S., M.E. and J.L. supervised the project. A.O., J.L. and S.K. conceived of the idea. A.O. and J.L. designed and carried out all of the electrochemical experiments. A.O. synthesized the catalysts and fabricated the electrodes and slim flow-cell electrolyser. A.O. performed the SEM, TEM and XPS measurements. S.L. performed the COMSOL simulations. S.K., V.S.K. and P.M.B. synthesized and characterized the Hex–Aza–COF nanosheets. Y.Z.F. performed the XAS measurements. Y.-K.W. performed the XRD measurements. X.-Y.L. performed the DFT calculations with the assistance of P.O. T.A., F.P.G.d.A. and A.H.I. contributed to data analysis. A.O. and J.L. cowrote the manuscript. D.S., E.H.S. and O.S. contributed to manuscript editing. All authors discussed the results and assisted during manuscript preparation.

Competing interests

The authors declare no competing interests.

Additional information

Supplementary information The online version contains supplementary material available at https://doi.org/10.1038/s41560-022-01188-2.

Correspondence and requests for materials should be addressed to Jun Li, Mohamed Eddaoudi, Edward H. Sargent or David Sinton.

Peer review information *Nature Energy* thanks Ezra Clark and the other, anonymous, reviewer(s) for their contribution to the peer review of this work.

Reprints and permissions information is available at www.nature.com/reprints.